Fluid Dynamics & Materials Processing
DOI:10.32604/fdmp.2020.09791
Article

Tech Science Press

RANS Simulation for the Maneuvering and Control of a Suboff Submarine Model

Jinyu Ren, Dezhi Xu and Jing Xu*

Naval Architecture and Ocean Engineering, Wuhan Technical College of Communications, Wuhan, 430065, China
*Corresponding Author: Jing Xu. Email: 308810953@qq.com
Received: 19 January 2020; Accepted: 23 April 2020

Abstract: Submarine maneuverability has been analyzed by means of computational fluid dynamics (CFD). This approach provides an alternative, accurate, and cost-effective method for simulating actual flow. The numerical results show that the numerical simulation of the viscous flow related to a moving submarine based on the RANS equation with a relevant turbulence model can not only provide rich flow field details such as flow separation, but also accurately predict its hydrodynamic performance. The present study indicates that CFD can be used to forecast the submarine's maneuverability in the initial design stage. The present results will be used in the future as a basis for analyzing methods to reduce the vibration and noise generated by the submarine.

Keywords: RANS equations; numerical simulations; suboff submarine model

1 Introduction

Maneuverability is an important navigation performance, which is closely related to navigation safety and tactical performance of submarine. At present, the real ship experiment method is the most reliable method for the study of submarine maneuverability. However, it usually has the disadvantages of long period, high cost, and difficulty in obtaining the flow details. Therefore, numerical simulation of submarine maneuverability has gained much interest. With the rapid development of computer technology and numerical methods, numerical simulation has attracted increasing attention in the research of submarine maneuverability. The SUBOFF standard model has been intensively investigated through experiments and calculations [1–3]. Reynolds number was investigated for the wing model, leading to some useful conclusions [4–7]. RANS simulation of viscous flow of fully appended submarine has been investigated [8]. Numerical prediction of submarine hydrodynamic coefficients by computational fluid dynamics (CFD) has been discussed [9]. Numerical simulation of flows over underwater axis symmetric bodies with full appendages has been researched [10]. The unsteady Reynolds averaged Navier-Stokes and large Eddy simulation of SUBOFF have been studied [11]. The effect of turbulence closure models on the vertical flow field around a prolate ellipsoid and submarine body undergoing steady drift has been considered [11,12].

The primary purpose of static measurements in these experiments is to obtain maneuvering forces and moments for developing and validating semiempirical or coefficient-based simulation methods and

validating CFD codes. In most cases, accurate determination of the drag or axial force is a secondary consideration.

This study has two objectives. The first is to make a general examination of the static data for a prolate ellipsoid to compare overall uncertainty with the $Sk-\omega$, $SSTk-\omega$, and k-ε models. However, differences in the procedures and experimental conditions, and differing degrees of details in the difference value analysis provided, preclude selection of the "best" set of data. The second objective is to compare selected static data and predictions from the SUBOFF standard model. These comparisons were made in the course of refining some of the hydrodynamic calculations in recent revisions of the code. These objectives are related to each other in that the development of semiempirical prediction methods invariably uses data from different sources. It is important to evaluate whether apparent inconsistencies arise from differences between facilities and procedures, or represent physical phenomenon that should be modeled, as much of the standard model database is proprietary to the various sponsors.

2 Mathematical Models

2.1 RANS Equations

The governing equations are the 3D uncompressible RANS equations [13]. Continuity equation and momentum equation in the tensorial expression can be written as:

$$\frac{\partial u_i}{\partial x_i}=0 \tag{1}$$

$$\frac{\partial(\rho u_i)}{\partial t}+\frac{\partial(\rho u_i u_j)}{\partial x_j}=f_i-\frac{\partial p}{\partial x_i}+\frac{\partial}{\partial x_j}\left[\mu\left(\frac{\partial u_i}{\partial x_j}+\frac{\partial u_j}{\partial x_i}\right)\right]-\frac{\partial(\rho\overline{u_i' u_j'})}{\partial x_j} \tag{2}$$

where u_i is the Cartesian $x_i(i=1,2,3)$velocity component, u_i' is the Fluctuating velocity component, and $\rho\overline{u'_i u'_j}$ indicates the Reynolds stress tensor.

2.2 $k-\varepsilon$ Turbulence Modeling

$k-\varepsilon$ model is widely used for pressure gradient solution due to its advantages of good stability and high precision.

$$\frac{\partial(\rho k)}{\partial t}+\frac{\partial(\rho u_j k)}{\partial x_j}=\frac{\partial}{\partial x_j}\left(\left(\mu+\frac{\mu_t}{\sigma_k}\right)\frac{\partial k}{\partial x_j}\right)+P_k-\rho\varepsilon \tag{3}$$

$$\frac{\partial(\rho\varepsilon)}{\partial t}+\frac{\partial(\rho u_j \varepsilon)}{\partial x_j}=\frac{\partial}{\partial x_j}\left(\left(\mu+\frac{\mu_t}{\sigma_\varepsilon}\right)\frac{\partial \varepsilon}{\partial x_j}\right)+\frac{\varepsilon}{k}(C_{\varepsilon 1}P_k-C_{\varepsilon 2}\rho\varepsilon) \tag{4}$$

$$P_k=\mu_t\frac{\partial u_i}{\partial x_j}\left(\frac{\partial u_i}{\partial x_j}+\frac{\partial u_j}{\partial x_i}\right) \tag{5}$$

$$\mu_t=C_\mu\rho\frac{k^2}{\varepsilon} \tag{6}$$

where ε is the turbulent kinetic energy dissipation rate and P_k is the turbulent kinetic energy term $C_\mu=0.09$, $C_{\varepsilon 1}=1.44$, $C_{\varepsilon 2}=1.92$, $\sigma_k=1.0$, $\sigma_\varepsilon=1.30$.

2.3 $k-\omega$ Turbulence Modeling

$k-\omega$ modeling is an empirical model, based on Wilcox's original model [14].

$$\frac{\partial}{\partial t}(\rho k)+\frac{\partial}{\partial x_i}(\rho k u_i)=\frac{\partial}{\partial x_j}\left[\left(\mu+\frac{u_t}{\sigma_k}\right)\frac{\partial k}{\partial x_j}\right]+G_k-Y_k \tag{7}$$

$$\frac{\partial}{\partial t}(\rho \omega)+\frac{\partial}{\partial x_i}(\rho \omega u_i)=\frac{\partial}{\partial x_j}\left[\left(\mu+\frac{u_t}{\sigma_\omega}\right)\frac{\partial \omega}{\partial x_j}\right]+G_\omega-Y_\omega \tag{8}$$

where G_k represents the production of turbulent viscosity, G_ω, Y_k, and Y_ω represent the dissipation of turbulent viscosity. $\sigma_k = 2.0$, $\sigma_\omega = 2.0$, $a_0 = 1/9$, $a_\infty = 0.52$.

2.4 $SSTk-\omega$ Turbulence Modeling

$SSTk-\omega$ modeling was developed by Menter et al., taking into account the orthogonal divergence. It has wide application and precision in the near-wall free flow.

$$\frac{\partial}{\partial t}(\rho k)+\frac{\partial}{\partial x_i}(\rho k u_i)=\frac{\partial}{\partial x_j}\left[\left(\mu+\frac{u_t}{\sigma_k}\right)\frac{\partial k}{\partial x_j}\right]+G_k-Y_k+S_k \tag{9}$$

$$\frac{\partial}{\partial t}(\rho \omega)+\frac{\partial}{\partial x_i}(\rho \omega u_i)=\frac{\partial}{\partial x_j}\left[\left(\mu+\frac{u_t}{\sigma_\omega}\right)\frac{\partial \omega}{\partial x_j}\right]+G_\omega-Y_\omega+S_\omega+D_\omega \tag{10}$$

where D_ω is the matrix parameter, and S_k and S_ω are the custom parameters.

3 Numerical Analysis and Validation

3.1 Numerical Model

The three-dimensional viscous flow was numerically simulated by the SUBOFF model. The other two models were processed by solving RANS equations with two-equation turbulence model and finite volume method, and with SIMPLEC method for pressure-linked terms, central difference schemes for temporal derivative terms, and second-order upwind schemes for convective and diffusive terms.

The numerical calculation of the three-dimensional flow field around a 6:1 ellipsoid was performed. The total length L of the ellipsoid is 4.356 m, the maximum diameter of the ellipsoid is 0.726 m, and the ratio of the major axis to the minor axis is 6:1, as shown in Fig. 1.

The inflow conditions and turbulence modes selected for the ellipsoid are as follows:

The inflow surface: The speed inlet boundary condition was adopted, and the inflow speed was 0.97 m/s.

The outflow surface: Free to flow out boundary condition was used.

The wall: No slip condition was used.

The turbulence mode: Reynolds number is 4.2×10^6. SIMPLE algorithm, second-order upwind scheme, and three turbulence modes of $Sk-\omega$, $SSTk-\omega$, and k-ε were selected for comparative analysis.

3.2 Analysis and Validation

Fig. 2 shows the three-dimensional flow separation diagram of an ellipsoid. The flow around the ellipsoid was numerically simulated with the angle of attack of 10° and 20°.

Figs. 3–6 show that the surface pressure distribution of the ellipsoid is consistent with the calculation results [13]. When the angle of attack of the ellipsoid is 10°, there is almost no flow separation. However, a sign of diversion is observed. When the angle of attack reaches 20°, the surface of the ellipsoid shows a second flow separation.

The hydrodynamic calculation results corresponding to different turbulence models of ellipsoids at the working angles of 10° and 20° are listed in Tab. 1.

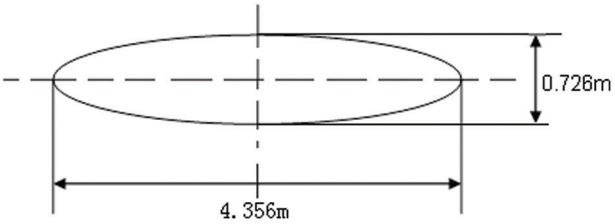

Figure 1: 6:1 ellipsoid

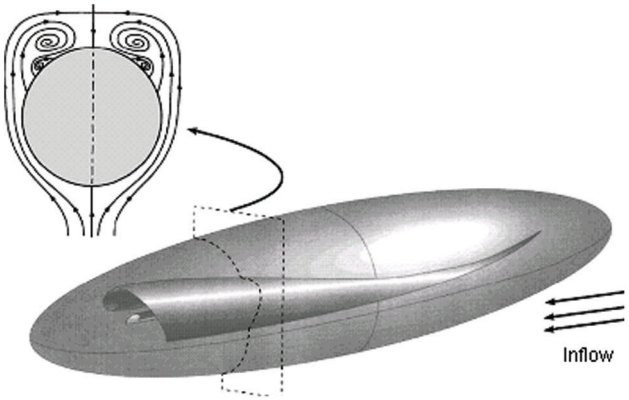

Figure 2: 3-D Flow separation diagram of 6:1 ellipsoid

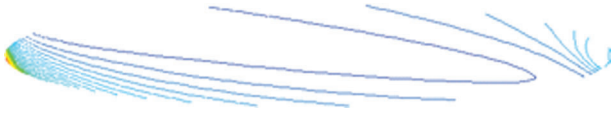

Figure 3: Pressure distribution on the surface of ellipsoid calculated in this study (a = 10°, Re = 4.2×10^6)

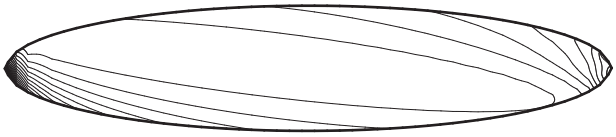

Figure 4: Pressure distribution on the surface of ellipsoid calculated in previous report [Pasinato (2002)] (a = 10°, Re = 4.2×10^6)

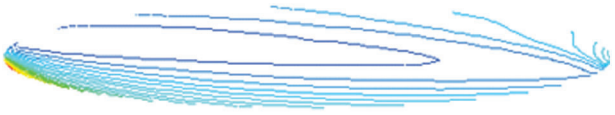

Figure 5: Pressure distribution on the surface of ellipsoid calculated in this study (a = 20°, Re = 4.2×10^6)

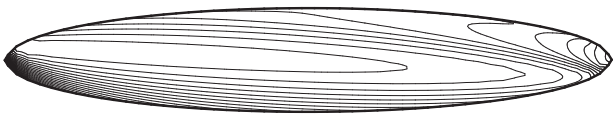

Figure 6: Pressure distribution on the surface of ellipsoid calculated in previous report [Pasinato (2002)] (a = 20°, Re = 4.2×10^6)

Table 1: Hydrodynamic calculation results of ellipsoid

turbulence models	$Z'(1\text{-}e^3)$	difference value	$M'(1\text{-}e^3)$	difference value
Experiment (a = 10°)	3.3099	–	−3.5862	–
$Sk-\omega$ (a = 10°)	3.0895	−6.5	−3.3102	−7.4
$SSTk-\omega$ (a = 10°)	2.9210	−11.0	−3.3201	−6.1
k-ε (a = 10°)	3.0306	−7.7	–3.4201	−7.0
Experiment (a = 20°)	13.169	–	–5.2676	–
$Sk-\omega$ (a = 20°)	15.012	9.5	−4.7032	−8.0
$SSTk-\omega$(a = 20°)	12.120	−8.1	−5.1230	−1.8
k-ε (a = 20°)	11.315	−12.8	−5.5236	3.6

Tab. 1 shows that the calculated results of the vertical force of each turbulence model are generally lower than the experimental values. When the angle of attack is 20°, the results of the vertical force are higher than the experimental values. This is because under the condition of high angle of attack, fluid flow separation occurs on the back flow surface when the fluid passes through the ellipsoid. Moreover, the separation shear layer presents two spirals, which generate additional lift to the ellipsoid. By comparing the vertical force, pitching moment, and the center position of the hydrodynamic action, it is found that the *Sk 2T* turbulence model exhibits good agreement with the experimental data [3].

4 Numerical Results and Analysis

The SUBOFF submarine model is a hull with a podium and a stabilizer wing, as shown in Fig. 7. The total length L of the hull, the length of the inflow section, the length of the parallel hull, the length of the outflow section, and the maximum diameter D are 4.356 m, 1.016 m, 2.229 m, 1.111 m, and 0.508 m, respectively. The podium enclosure is 0.368 m long and 0.460 m high. The leading edge of the podium is located at 0.924 m, and the trailing edge is located at 1.923 m. The stabilizer wing is arranged in a cross shape with the trailing edge of the wing at 4.007 m. The specific geometry of the SUBOFF model is from DAPRA [3].

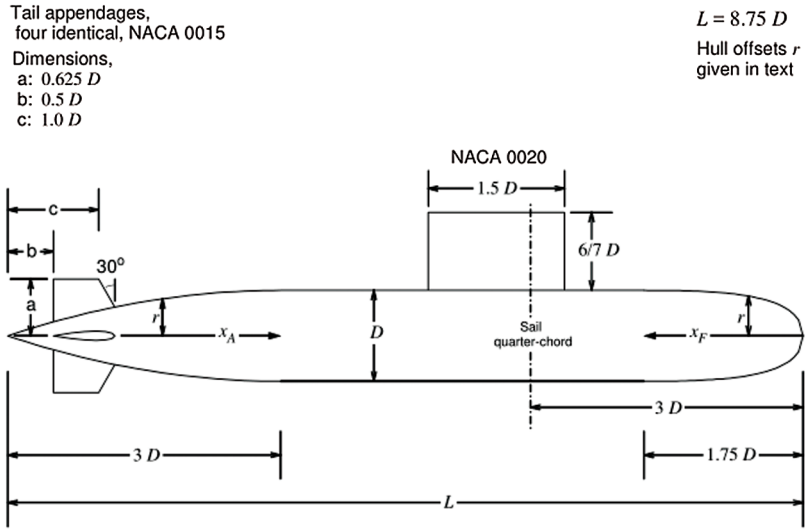

Figure 7: SUBOFF model

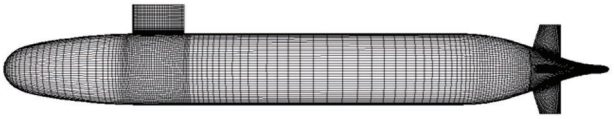

Figure 8: Surface grid of SUBOFF

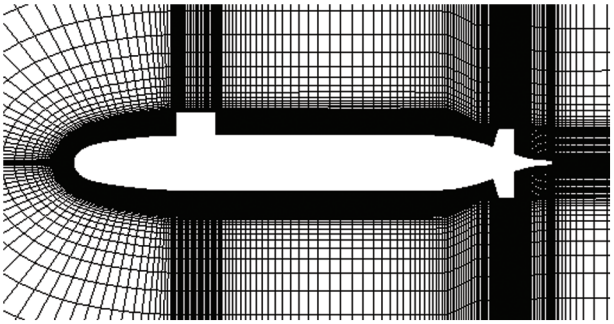

Figure 9: Flow grid of SUBOFF model

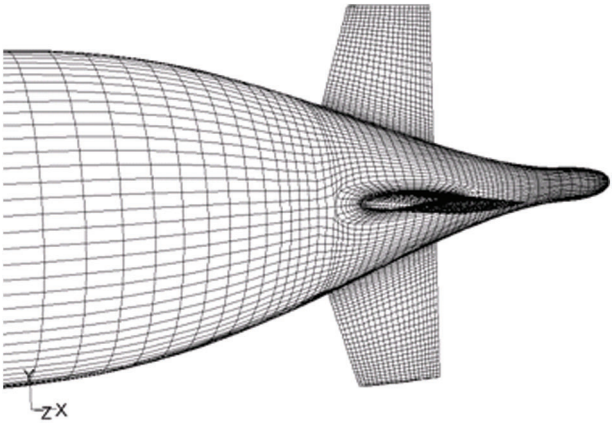

Figure 10: The rear wing grid of SUBOFF model

The SUBOFF full-appendage model including a podium enclosure and cross-shaped tail is shown in Fig. 8. The podium and the tail of the SUBOFF model were made of grids to capture the flow field characteristics near the podium and the tail. Fig. 9 shows the flow field grid around the SUBOFF model and Fig. 10 shows the rear wing grid.

4.1 The Inflow Conditions

The larger the selected calculation domain, the closer would be the calculation model under the unbounded flow circumstance, and the more accurate would be the result. However, the larger the amount of calculation, the larger the error. If the calculation area is too small, the boundary conditions may not be established, and it would be difficult to guarantee the correctness of the results. Therefore, the selected calculation area length is five times longer than the model, and the width is three times longer than the model.

Tab. 2 shows the results of mesh sensitivity analysis. It can be seen that the values of vertical force and moment change with the number of meshes. When the Reynolds number is 1.3×10^7, the submarine model has an attack angle of 12°, and the number of grids is increased from 2 to 3.5 million. At this point, the values

Table 2: Mesh sensitivity analysis

Number of fluid cells	$X'(1\text{-}e^3)$	$Z'(1\text{-}e^3)$	$M'(1\text{-}e^3)$
515690	0.8223	3.0562	−2.5263
1025782	0.9042	3.1869	−2.6562
2052744	0.9145	3.4953	−2.7356
3562176	0.9182	3.5025	−2.7897

of vertical force and moment are relatively stable and do not change significantly. Thus, it is feasible to choose 2 million grids.

The inflow conditions and turbulence modes selected for the SUBOFF model are as follows:

The inflow surface: The speed inlet boundary condition was adopted, and the inflow speed was 2.1 m/s.

The outflow surface: Free flow out boundary conditions.

The wall: No slip conditions.

The turbulence mode: Reynolds number is 1.3×10^7. SIMPLE algorithm, second-order upwind scheme, and $Sk - \omega$ turbulence models were selected for comparative analysis.

The inflow surface is a semi-sphere and cylinder, the outlet surface is the back end of the cylinder, and the wall surface is the surface of the submarine, as shown in Fig. 11.

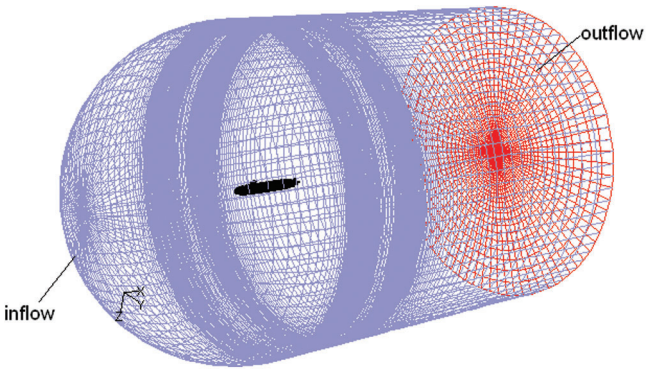

Figure 11: Computational domain of flow field

4.2 Numerical Analysis

Fig. 12 shows the simulation of the surface pressure distribution of the SUBOFF full attachment, which reflects the pressure distribution on the surface of the submarine well. The pressure coefficient is likely caused by the low flow velocity in these areas.

Figs. 13 and 14 show the comparison diagrams of the longitudinal section pressure coefficient and longitudinal section friction coefficient with the experimental values, respectively. These calculated values are in good agreement with the reported experimental values [2].

Figs. 15 and 16 present the surface pressure distribution diagrams of a fully attached submarine when the Reynolds number is 1.3×10^7, and the submarine model has an attack angle of −4° and 8°. It can be seen that the pressure on the submerged surface is significantly greater than the pressure on the leeward surface.

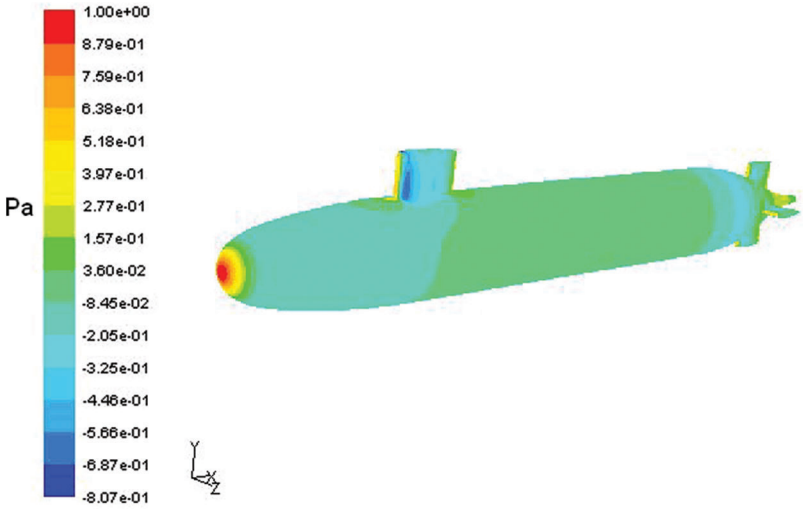

Figure 12: Surface pressure of fully attached SUBOFF (a = 0°)

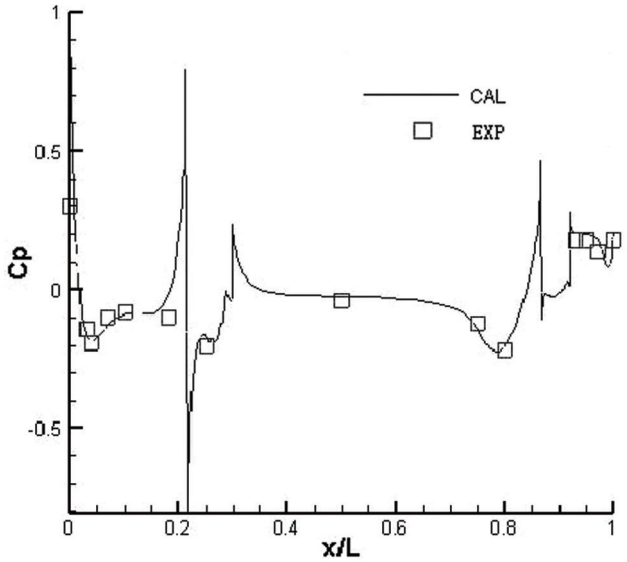

Figure 13: Profile pressure coefficient curve of the longitudinal section of fully attached SUBOFF

Figs. 17 and 18 present the streamline diagrams of the near surface of a fully attached submarine when the submarine model has an attack angle of 8° and 14°, respectively. The figures show the complex vortices near the submarine's control platform and the tail.

Tab. 3 shows the results of hydrodynamic calculations of a fully attached submarine ($Re = 1.3 \times 10^7$, −12° to 12°). It can be seen that the deviation between the numerical simulation results and the experimental values is less than 4%. Figs. 19 and 20 show the comparison charts between the calculated vertical force coefficient and the pitching moment coefficient curve and the experimental values. The numerical simulation curve agrees well with the experimental curve [14,15].

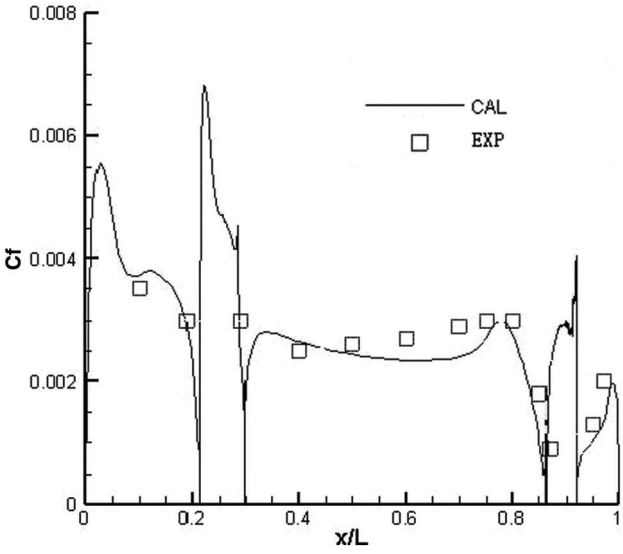

Figure 14: Friction coefficient curve of the longitudinal section of fully attached SUBOFF

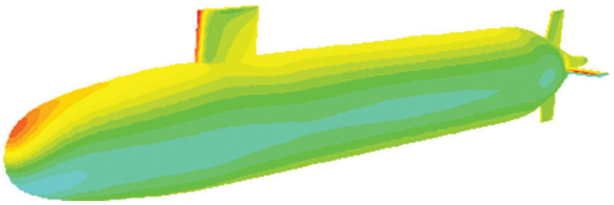

Figure 15: Surface pressure of fully attached SUBOFF (a = −4°, Re = 1.3×10^7)

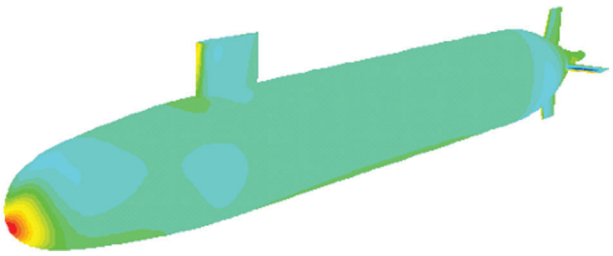

Figure 16: Surface pressure of fully attached SUBOFF (a = 8°, Re = 1.3×10^7)

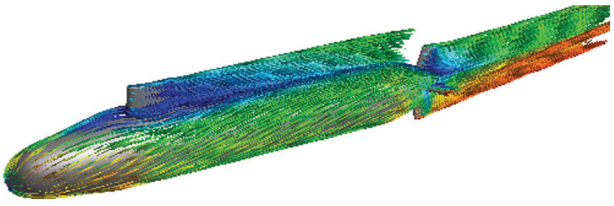

Figure 17: Surface streamline of fully attached SUBOFF (a = 8°, Re = 1.3×10^7)

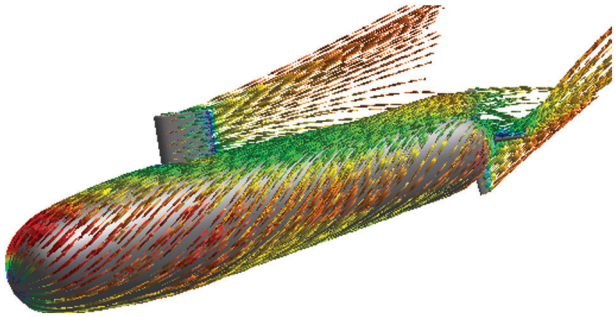

Figure 18: Surface streamline of fully attached SUBOFF (a = 14°, Re = 1.3 × 10^7)

Table 3: SUBOFF full appendage hydrodynamic calculation results (Re = 1.3 × 10^7)

Hydrodynamic derivative	Experiment value	Calculated value	Difference value
Z'_w	−0.01105	−0.01051	−3.91
M'_w	0.01082	0.01045	−4.02
$Z'_{w\|w\|}$a= −12°~+12°	−0.04528	−0.04823	3.2
$M'_{w\|w\|}$a = −12°~+12°	−0.01203	−0.01008	5.4

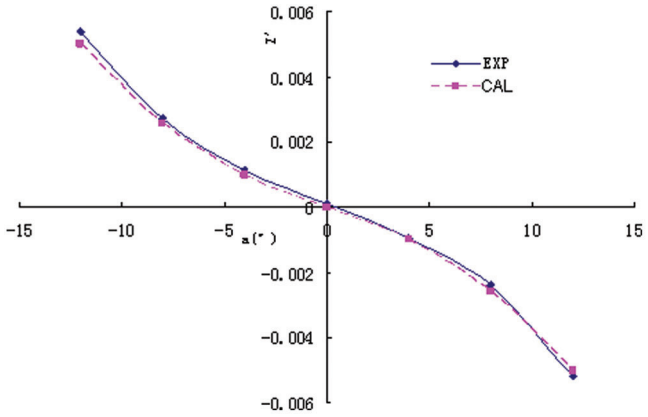

Figure 19: Curve of vertical force coefficient of fully attached submarine with variable angle of attack

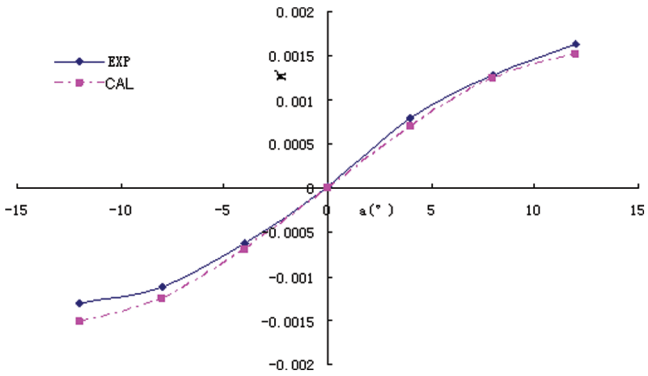

Figure 20: Pitch moment coefficient curve of fully attached submarine with variable angle of attack

5 Conclusions

In this work, turbulent three-dimensional viscous flow around an ellipsoid was numerically compared with different turbulence models, and the hydrodynamic forces were calculated. The calculated results were in good agreement with the previously reported experimental data.

Numerical simulations were carried out for the main hull of the SUBOFF submarine with sail on the top in maneuvering motions. The simulated flow details and computed hydrodynamic forces and moments were in good agreement with the experimental data.

In order to evaluate the hydrodynamic performance of the submarine stern appendages, the viscous flow around the foil was studied by numerical simulation, and the results were found to be consistent with the experimental data. This work demonstrates that the use of a solver based on the RANS equation to numerically simulate the viscous flow of a moving submarine can not only provide rich flow field details such as flow separation, but also accurately predict its hydrodynamic performance.

The initial design stage of the submarine can be used to predict the submarine's maneuverability, which can provide a basis for the analysis and research of the vibration and noise reduction of the submarine.

Acknowledgement: This work was supported by Ministry of Education of the People's Republic of China.

Funding Statement: This work was supported by Scientific Research Fund of Ministry of Education Innovation platform open fund Project (No. 2018C01044) and (No. 2018A03025).

Conflicts of Interest: The authors declare that they have no conflicts of interest to report regarding the present study.

References

1. Joubert, R. N. (2006). *Some aspects of submarine design: shape of a submarine*. Australian Government: Defense Science and Technoloy Organization.
2. Cindy, C. W. (1999). Steady and unsteady force and moment data on a DARPA2 submarine. *Master of Science in Aerospace Engineering, 5(2),* 102–119.
3. Groves, N. C., Huang, T. T., Chang, M. S. (1989). *Geometric characteristics of DARPA SUBOFF models*. Washington, DC: David Taylor Research Center.
4. Abbassi, A., Kechiche, N., Aissia, H. B. (2014). Low Reynolds numbers LDA-experimental analysis of the near-field of an isothermal laminar round free jet. *Fluid Dynamics & Materials Processing, 10(3),* 319–341.
5. Bourantas, G., Skouras, E., Loukopoulos, V., Nikiforidis, G. (2010). Meshfree point collocation schemes for 2D steady state incompressible Navier-Stokes equations in velocity-vorticity formulation for high values of Reynolds number. *Computer Modeling in Engineering & Sciences, 59(1),* 31–64.
6. Han, Y., Chen, D., Liu, S., Xu, G. (2020). An investigation into the effects of the Reynolds number on high-speed trains using a low temperature wind tunnel test facility. *Fluid Dynamics & Materials Processing, 16(1),* 1–19. DOI 10.32604/fdmp.2020.06525.
7. Guo, S., Chen, S., Huang, X., Zhang, Y., Jin, S. (2014). CFD and experimental investigations of drag force on spherical leak detector in pipe flows at high Reynolds number. *Computer Modeling in Engineering & Sciences, 101(1),* 59–80.
8. Yang, Q. F., Wang, Y., Zhang, Z. (2012). RANS simulation of viscous flow over full appended submarine and field variables walidation and vorticity analysis. *Chinese Journal of Computation Mechanics, 29(4),* 567–573.
9. Pan, Z. Y., Wu, B. S., Shen, H. C. (2004). Research of CFD application in engineering estimation of submarine maneuverability hydrodynamic forces. *Journal of Ship Mechanics, 8(5),* 42–51.
10. Huang, Z., Zhou, L. D. (2001). Numerical simulation of flows over underwater axis symmetric bodies with full appendages. *Shipbuilding of China, (1),* 4–13.

11. Xue, D. Q. (2016). Analysis on orthogonal optimization of cooling pump in agricultural vehicle based on CFD. *Journal of Chinese Agricultural Mechanization, 37(9),* 135–139.
12. Alexander, B. (2010). Influence of turbulence closure models on the vortical flow field around a submarine body undergoing steady drift. *Journal of Marine Science and Technology, 15(3),* 201–217. DOI 10.1007/s00773-010-0090-1.
13. Pasinato, H., Wang, Y. Q. (2002). Numerical investigation of flow past a prolate spheriod. *Journal of Fluids Engineering, 124(4),* 904–910. DOI 10.1115/1.1517571.
14. Coutier, D. O., Reboud, J. L., Delannoy, Y. (2003). Numerical simulation of the unsteady behaviour of cavitating flows. *International Journal for Numerical Methods in Fluids, 8(4),* 115–120.
15. Qiu, L. Y., Shi, Z. K., Hou, G. X. (2007). Validation of numerical simulation of the flow over submarine geometries with full appendages. *Journal of Ship Mechanics, 11(3),* 341–350.